

Intertwined Dirac cones induced by anisotropic coupling in antiferromagnetic topological insulator

Yiliang Fan¹, Huaiqiang Wang^{2,*}, Peizhe Tang^{3,4}, Shuichi Murakami⁵, Xiangang Wan^{1,6}, Haijun Zhang^{1,6,*}, and Dingyu Xing^{1,6}
¹ National Laboratory of Solid State Microstructures and School of Physics, Nanjing University, Nanjing 210093, China
² School of Physics and Technology, Nanjing Normal University, Nanjing 210023, China
³ School of Materials Science and Engineering, Beihang University, Beijing 100191, China
⁴ Max Planck Institute for the Structure and Dynamics of Matter, Center for Free Electron Laser Science, Hamburg 22761, Germany
⁵ Department of Physics, Tokyo Institute of Technology, Tokyo 152-8551, Japan
⁶ Collaborative Innovation Center of Advanced Microstructures, Nanjing University, Nanjing 210093, China

Antiferromagnetic topological insulators (AFM TIs), which host magnetically gapped Dirac-cone surface states and exhibit many exotic physical phenomena, have attracted great attention. The coupling between the top and bottom surface states becomes significant and plays a crucial role in its low-energy physics, as the thickness of an AFM TI film decreases. Here, we find that the coupled surface states can be intertwined to give birth to a set of $2n$ brand new Dirac cones, dubbed *intertwined Dirac cones*, through the anisotropic coupling due to the n -fold crystalline rotation symmetry C_{nz} ($n = 2, 3, 4, 6$) in the presence of an out-of-plane electric field. Interestingly, we also find that the warping effect further drives the intertwined Dirac-cone state into a quantum anomalous Hall phase with a high Chern number ($C = n$). Then, we demonstrate the emergent six intertwined Dirac cones and the corresponding Chern insulating phase with a high Chern number ($C = 3$) in $\text{MnBi}_2\text{Te}_4/(\text{Bi}_2\text{Te}_3)_m/\text{MnBi}_2\text{Te}_4$ heterostructures through first-principles calculations. This work discovers a new intertwined Dirac-cone state in AFM TI thin films and also reveals a new mechanism for designing the quantum anomalous Hall state with a high Chern number.

I. INTRODUCTION

The interplay between magnetism and topology in condensed matters has greatly enriched the research content of topological quantum physics with many exotic physical phenomena, such as quantum anomalous Hall effect (QAHE) [1–5], magnetic Weyl semimetals [6, 7], topological magnetoelectric effects [8, 9], axion polariton [10–13] and so on. Recently, MnBi_2Te_4 and its family were discovered to be an important class of promising intrinsic magnetic topological insulators (TIs) and have attracted great attention [14–38]. As the most representative material, MnBi_2Te_4 , having the A-type antiferromagnetic (AFM) ground state, is found to be a static axion insulator with quantized magnetoelectric effect [16, 30]. Moreover, the QAHE with a high temperature (~ 1 K, higher than that of Cr-doped $(\text{Bi,Sb})_2\text{Te}_3$ films [3]) was theoretically proposed and experimentally observed in odd-septuple-layer (SL) MnBi_2Te_4 films [4, 16, 17, 22], and the dynamical topological magnetoelectric effect was theoretically proposed in even-SL MnBi_2Te_4 films [39]. Most interestingly, the layer Hall effect was also demonstrated in even-SL MnBi_2Te_4 films in which there are two separated magnetically gapped Dirac cones exhibiting half-

integer quantized Hall conductivity with opposite signs ($\pm e^2/2h$) on the top and bottom surfaces [33].

When the thickness of such a AFM TI film is gradually reduced, the two separated Dirac-cone surface states become coupled with each other. This coupling could play a crucial role especially in an ultrathin (< 10 nm) AFM TI film. For example, the competition between the surface-state coupling and magnetic order can lead to a topological phase transition between a trivial phase and a QAHE [2, 40]. Generally speaking, on account of the n -fold ($n = 2, 3, 4, 6$) crystalline rotation symmetry (C_{nz}) that a (magnetic) TI usually respects, the surface-state coupling should contain both isotropic terms and symmetry-allowed anisotropic terms [41]. However, to our knowledge, only isotropic surface-state couplings are considered [40, 42–46], whereas anisotropic couplings are simply omitted.

Remarkably, in this work, we find that the C_{nz} -symmetry-allowed anisotropic coupling can induce a set of $2n$ brand new Dirac cones, termed intertwined Dirac cones, around the Γ point through intertwining the two original Dirac cones on the top and bottom surfaces of AFM TI thin films in the presence of a PT -symmetry breaking potential, e.g. an out-of-plane

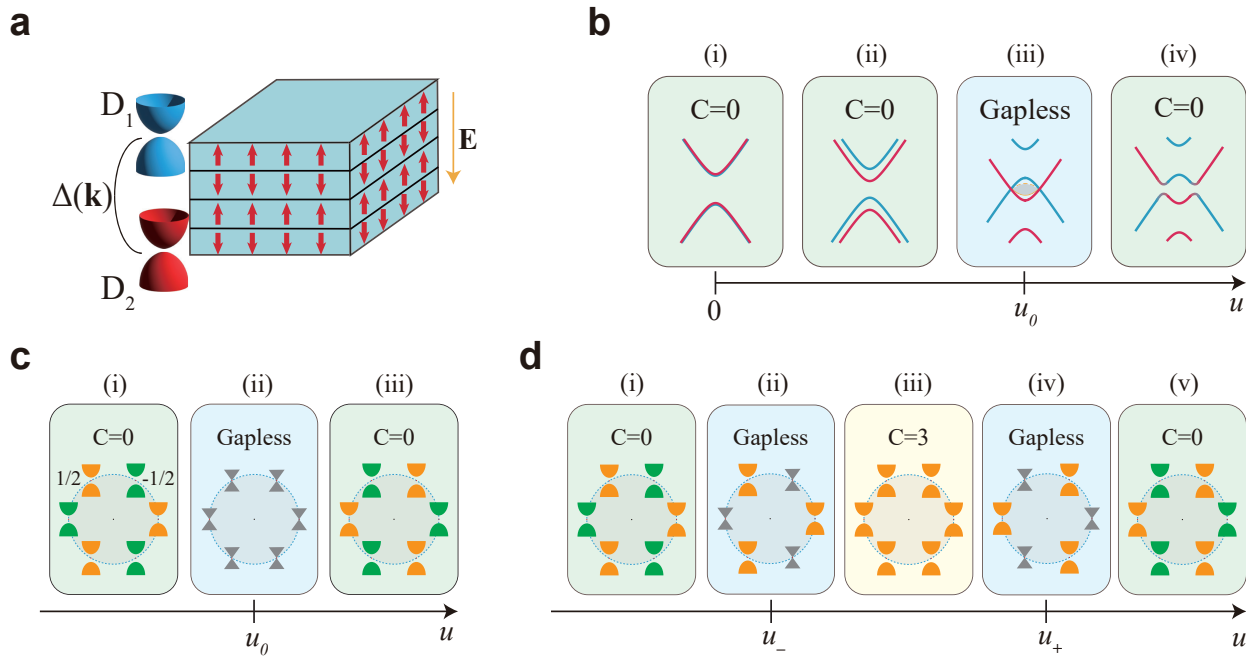


FIG. 1: **Schematic of intertwined Dirac cones and high-Chern-number phase transition.** (a) The coupled top and bottom Dirac-cone surface states of an AFM TI thin film. (b) The surface states are doubly degenerate when the PT symmetry is preserved (i). An external electric field can shift the surface Dirac cones to split the degenerate bands (ii). When only considering the isotropic coupling (see the main text for the details), the energy gap first closes with a gapless nodal ring at $u = u_0$ (iii) and reopens (iv), but without a topological transition. (c) When introducing the symmetry-allowed anisotropic coupling, the gapless nodal ring splits into six intertwined Dirac cones if the AFM TI film has a 3-fold rotation symmetry. The color of Dirac cones indicates the different Chern number, with green (orange) representing $C = -1/2$ ($C = 1/2$). Green and orange Dirac cones simultaneously change their signs across the gapless point, with increasing the electric field, but there is still no topological transition. (f) When further considering the symmetry-induced warping effect, the three green intertwined Dirac cones first change their sign from $C = -1/2$ to $C = 1/2$ at $u = u_-$ (ii) to result in a topological transition to a $C = 3$ phase (iii), and as the electric field increases, the other three orange intertwined Dirac cones change their sign from $C = 1/2$ to $C = -1/2$ at $u = u_+$ (iv) to make the second topological transition to $C = 0$ (v).

electric field. More intriguingly, when further taking the symmetry-allowed warping effect into consideration, an electrically tunable high-Chern-number ($|C| = n$) QAHE can appear. These are further explicitly verified by the existence of six intertwined Dirac cones and the corresponding $|C| = 3$ Chern insulating phase in $\text{MnBi}_2\text{Te}_4/(\text{Bi}_2\text{Te}_3)_m/\text{MnBi}_2\text{Te}_4$ ($m = 0, 1, 2$) heterostructures through first-principles calculations, and also confirmed in HgS films with the C_{2z} rotation symmetry and $\alpha\text{-Ag}_2\text{Te}$ films with the C_{4z} rotation symmetry [47, 48], by introducing the magnetic proximity effect on the surfaces. This work not only reveals a new concept of intertwined Dirac cones in AFM TI films, but also provides a new scheme to achieve high-Chern-number QAHE.

II. INTERTWINED DIRAC-CONE STATES

We start from an even-layer AFM TI thin film with two Dirac-cone surface states located on the top and bottom

surfaces, respectively, as illustrated in Fig. 1a. Due to the out-of-plane surface magnetic moments, if the two Dirac-cone surface states are uncoupled, each of them can be described by a Dirac-cone Hamiltonian [41]

$$H_{D_\alpha} = \hbar v(k_x \sigma_y - k_y \sigma_x) + m_\alpha \sigma_z \quad (1)$$

where $\alpha = 1, 2$, D_1 (D_2) represents the top (bottom) Dirac cone, v is the Fermi velocity, $s = +(-)$ for the Dirac cone D_1 (D_2), the Planck's constant \hbar is simply set as 1 henceforth, and m_α indicates Zeeman coupling. Since magnetic moments on the two surfaces are opposite in the AFM TI, we have $m_1 = -m_2 = m$ (m is set to be positive henceforth). In the basis of $|D_1, \uparrow\rangle, |D_1, \downarrow\rangle, |D_2, \uparrow\rangle, |D_2, \downarrow\rangle$, where \uparrow (\downarrow) represent the spin, a four-band low-energy Hamiltonian of the two decoupled Dirac cones is directly written as:

$$H_0 = v\tau_z \otimes (k_x \sigma_y - k_y \sigma_x) + m\tau_z \otimes \sigma_z. \quad (2)$$

Here, the Pauli matrix τ_z acts in the subspace of top and bottom Dirac cones. This Hamiltonian describes two degenerate Dirac cones with a gap of $2m$, as shown

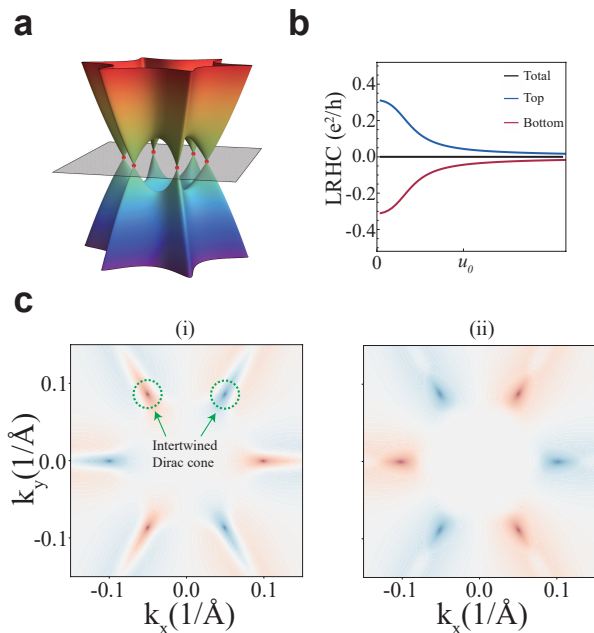


FIG. 2: **Intertwined Dirac-cone states and Berry curvatures induced by the anisotropic coupling with a 3-fold rotation symmetry.** (a) The six gapless intertwined Dirac cones at the critical electric field $u = u_0$. (b) The layer-resolved Hall conductivity (LRHC) for the top (blue line) and bottom (red line) surfaces with increasing the electric field. (c) The Berry curvatures for $u < u_0$ (i) and $u > u_0$ (ii), respectively. The significant Berry curvature is mainly located around the six intertwined Dirac cones, which changes sign from $u < u_0$ to $u > u_0$. The parameters are chosen as $m = 0.05$ eV, $v = 1$ eV \cdot \AA , $\Delta = 0.05$ eV, $B = 5$ eV \cdot \AA^2 , $R_1 = 100$ eV \cdot \AA^3 in the above numerical calculations.

in Fig. 1b(i). Note that although the time-reversal ($T = i\sigma_y K$ with K denoting the complex conjugate) and inversion ($P = \tau_x$) symmetries are separately broken, the combined PT symmetry of them is preserved, which ensures the double degeneracy of each band.

Based on H_0 , we then introduce a PT -symmetry breaking potential u between the two Dirac cones described by $H_u = u\tau_z \otimes \sigma_0$, which could be induced by an out-of-plane electric field ($u \propto E$). This potential lifts the double degeneracy of each band by shifting the two Dirac cones in opposite directions [see Fig. 1b(ii)], and it is indispensable for the realization of layer Hall effect [33]. With increasing u , the energy gap gradually reduces until it closes at the Γ point when $u = m$. If we continue to increase u , i.e. $u > m$, the closing point evolves into a gapless nodal ring with radius $\sqrt{u^2 - m^2}/v$ around the Γ point.

Now we consider the coupling between D_1 and D_2 . When assuming that the AFM TI respects C_{nz} ($n = 2, 3, 4, 6$) rotation symmetry and a combined symmetry $M_x T$ of mirror and time-reversal operations, we can obtain the following coupling Hamiltonian [see the supple-

mentary material (SM) [49] for more details]

$$H_{\text{coup}} = (\Delta - Bk^2)\tau_x \otimes \sigma_0 + R_1 g_n(k_x, k_y)\tau_y \otimes \sigma_0 \quad (3)$$

where $k^2 = k_x^2 + k_y^2$ and $g_n(k_x, k_y) = (k_+^n - k_-^n)/2i$ with $k_{\pm} = k_x \pm ik_y$, and i is the imaginary unit. The first term in Eq. (3) describes the isotropic couplings up to k^2 order ($\Delta B > 0$ is assumed throughout the work [43]), while the second term comes from the symmetry-allowed anisotropic coupling (for simplicity we have dropped other higher-order coupling terms which will not affect our main results [49]). Most importantly, it plays a crucial role in generating the intertwined Dirac-cone states, as we will show below. Without the anisotropic coupling, the energy gap only closes along a gapless nodal ring with the radius $k_0 = \sqrt{\Delta/B}$ at $u = u_0 = \sqrt{m^2 + v^2\Delta/B}$ [see Fig. 1b(iii)], and it reopens when $u > u_0$ [see Fig. 1b(iv)]. However, there is no topological phase transition in this gap-closing-and-reopening process, for the Chern number remains as zero. Interestingly, in the presence of the anisotropic coupling, it is found that the gapless nodal ring at $u = u_0$ splits into $2n$ nodal points connected to each other by C_{nz} symmetry, as illustrated in Fig. 1c(ii). In the k - θ polar coordinate (the original k_x -direction is chosen as the $\theta = 0$ direction), the $2n$ nodal points are located at (k_0, θ_j) , where $\theta_j = j\pi/n$, with $j = 0, 1, 2, \dots, 2n - 1$. Only at these nodal points, the coupling becomes zero, and to have a better knowledge of them, we expand the Hamiltonian around them to linear order and obtain an effective two-band Dirac-like Hamiltonian as

$$h_n(\theta_j) = -2Bk_0q_\rho\sigma_x + (-1)^j nR_1k_0^{n-1}q_\theta\sigma_y + \delta u\sigma_z \quad (4)$$

where $q_\rho = k - k_0$ and $q_\theta = k_0\delta\theta$ with $\delta\theta = \theta - \theta_j$, are the momentum measured from the nodal points along the radial and angular directions in the polar coordinates and $\delta u = u - u_0$. The effective Hamiltonian $h_n(\theta_j)$ indicates that each nodal point is a new Dirac-cone state with a mass of δu . Since this set of Dirac-cone states emerge from the coupling between the top and bottom local Dirac-cone surface states, they are dubbed “intertwined” Dirac-cone states. Moreover, according to Eq. (4), the helicity of the intertwined Dirac-cone state labeled by odd or even value of j is opposite. As a result, the Chern number for each intertwined Dirac-cone state, given by $C(\theta_j) = \frac{(-1)^{j+1}}{2}\text{sgn}(\delta u)$, turns out to be opposite for odd and even j [see Fig. 1c(i)]. It follows that when δu changes from negative ($u < u_0$) to positive ($u > u_0$), the Chern number changes by $+1$ (-1) for odd (even) j , as can be seen from Fig. 1c(iii), so the total Chern number still equals zero. To exemplify this, we have chosen $n = 3$ to numerically calculate the typical Berry curvature distribution of the valence bands near the transition point with $u < u_0$ [Fig. 2c(i)] and $u > u_0$ [Fig. 2c(ii)], as well as the band structure of the gapless intertwined Dirac-cone

states at the transition point of $u = u_0$ (Fig. 2a). Obviously, the local Berry curvature around each intertwined Dirac-cone state changes its sign between $u < u_0$ and $u > u_0$, and it is always opposite for intertwined Dirac-cone states characterized by odd and even j , leading to a zero net Chern number.

Furthermore, we have also investigated how the layer Hall effect is affected by the coupling between surface states. In Fig. 2(b), we have plotted the layer-resolved Hall conductivity (LRHC) as a function of the potential difference u . It can be seen that with increasing u , the LRHCs of both surfaces gradually decrease towards zero. Note that the deviation from the quantized value $\pm e^2/2h$ before the gap closing ($u < u_0$) results from the coupling between the surface states.

III. WARPING EFFECT AND HIGH-CHERN-NUMBER PHASE

Based on the above analysis concerning the intertwined Dirac-cone states, we are now ready to reveal the emergence of a high-Chern-number phase with $|C| = n$ by further considering the symmetry-induced warping effect [50, 51] of the two original Dirac-cone surface states. The warping effect can be described by the following Hamiltonian

$$H_{\text{warp}} = R_2 w_n(k_x, k_y) \tau_z \otimes \sigma_z, \quad (5)$$

where $w_n(k_x, k_y) = (k_+^n + k_-^n)/2$. Because of H_{warp} , the critical potential u_0 of the gap-closing condition for each intertwined Dirac-cone state now becomes [49]

$$u_{0,j} = \sqrt{\left[m + (-1)^j R_2 (\Delta/B)^{n/2} \right]^2 + v^2 \Delta/B}. \quad (6)$$

In contrast to the case without the warping effect where $u_{0,j}$ is the same for all values of j , the critical gapless transition point is now distinct between odd and even values of j , namely, $u_{0,j} \equiv u_-$ and u_+ for odd and even j , respectively. This can be understood from the fact that H_{warp} effectively introduces opposite corrections to the Zeeman term between intertwined Dirac cones with odd and even j . The difference between u_{\pm} indicates that the changes of Chern number ΔC of the intertwined Dirac-cone states with odd j ($\Delta C = +1$) and even j ($\Delta C = -1$) no longer occur simultaneously [see Figs. 1d(ii) and 1d(iv)]. As a result, if $mR_2 > 0$ is assumed, we have $u_- < u_+$ and a high-Chern-number phase with $C = n$ when $u_- < u < u_+$, while $C = 0$ for both $u > u_+$ and $u < u_-$, as schematically shown by the $C = 3$ case in Fig. 1d.

As further support, we have chosen $n = 3$ to numerically calculate the typical Berry curvature distribution of the valence bands with $u < u_-$ [Fig. 3c(i)], $u_- < u < u_+$ [Fig. 3c(ii)], and $u > u_+$ [Fig. 3c(iii)]. The band structures at the critical transition points of $u = u_-$ and

$u = u_+$ are presented in Figs. 3a(i) and 3a(ii), respectively. The sign change of the Berry curvature around each intertwined Dirac-cone state across the transition points of u_{\pm} can be clearly seen in Fig. 3c. Moreover, to verify that $u_- < u < u_+$ is indeed a high-Chern-number phase, we have explicitly calculated the anomalous Hall conductivity (AHC) in Fig. 3b, where the AHC indeed equals $3 e^2/h$ when the Fermi energy lies in the gap for $u_- < u < u_+$.

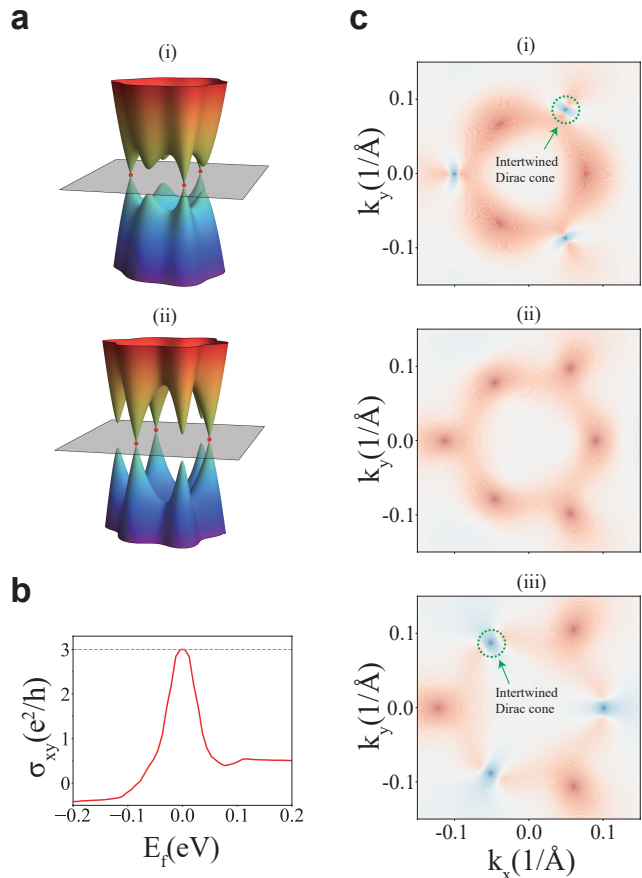


FIG. 3: **The high-Chern-number phase transition induced by the anisotropic coupling and the warping effect with a 3-fold rotation symmetry.** (a) The two successive band gap closings with the gapless intertwined Dirac cones at $u = u_-$ and $u = u_+$, respectively. (b) The anomalous Hall conductivity (AHC) for the $u_- < u < u_+$ case, where the AHC takes the quantized value of $3 e^2/h$ when the Fermi level lies in the energy gap. (c) Typical Berry curvatures for three different cases of $u < u_-$ (i), $u_- < u < u_+$ (ii), and $u > u_+$ (iii), respectively. The $u_- < u < u_+$ case represents the high-Chern-number phase with $C = 3$, and the other two cases represent the topologically trivial phases with $C = 0$. The parameters are chosen as $m = 0.05$ eV, $v = 1$ eV $\cdot \text{\AA}$, $\Delta = 0.05$ eV, $B = 5$ eV $\cdot \text{\AA}^2$, $R_1 = 100$ eV $\cdot \text{\AA}^3$, $R_2 = 100$ eV $\cdot \text{\AA}^3$ in the above numerical calculations.

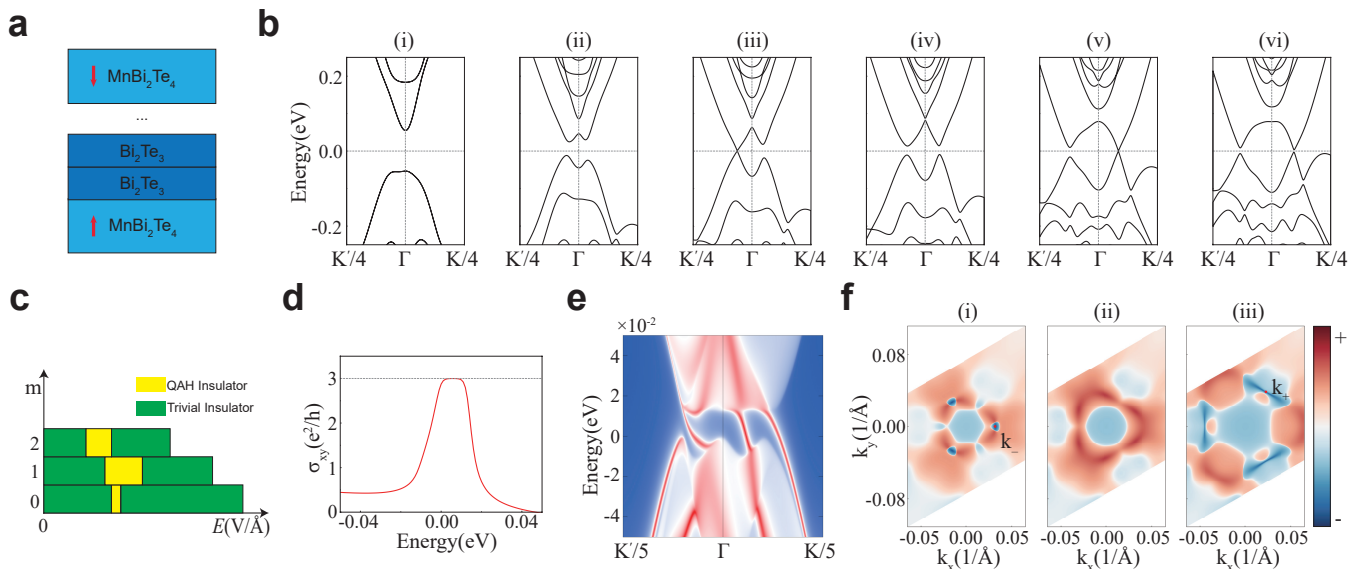


FIG. 4: **Intertwined Dirac cones and high-Chern-number phase in $\text{MnBi}_2\text{Te}_4/(\text{Bi}_2\text{Te}_3)_m/\text{MnBi}_2\text{Te}_4$ ($m = 0, 1, 2$) heterostructures** (a) The schematic heterostructure structure. (b) The band structure for the heterostructure with $m = 1$ under increasing the electric field, with $E = 0.0 \text{ V/\AA}$ (i), 0.008 V/\AA (ii), 0.0113 V/\AA (iii), 0.0135 V/\AA (iv), 0.0182 V/\AA (v), 0.02 V/\AA (vi). (c) The topological phase diagram as a function of the Bi_2Te_3 layer number and the electric field, where the yellow (green) region denotes the topologically nontrivial (trivial) phase with the Chern number $C = 3$ ($C = 0$). (d,e) The AHC as a function of the energy level for the $C = 3$ phase at $E = 0.0135 \text{ V/\AA}$ for $m = 1$. A quantized value of $\sigma_{xy} = 3 e^2/h$ can be seen when the energy level is in the energy gap, which originates from the emergence of three chiral edge states shown in (e). (f) Typical Berry curvatures for the three different insulating phases, namely, $E = 0.011 \text{ V/\AA}$ (the $C = 0$ phase before the first gap closing) (i), $E = 0.0135 \text{ V/\AA}$ (the intermediate $C = 3$ phase) (ii), and $E = 0.0186 \text{ V/\AA}$ (the $C = 0$ phase after the second gap closing) (iii), where significant changes of Berry curvatures are seen around the intertwined Dirac cones located at k_- (k_+) in the first (second) topological phase transition.

IV. MATERIAL REALIZATION

Inspired by recent experimental progresses on MnBi_2Te_4 family intrinsic AFM TIs and related heterostructures, such as MnBi_4Te_7 and $\text{MnBi}_6\text{Te}_{10}$ [25, 52–60], we take the $\text{MnBi}_2\text{Te}_4/(\text{Bi}_2\text{Te}_3)_m/\text{MnBi}_2\text{Te}_4$ ($m = 0, 1, 2$) heterostructure as a realistic example of the preceding $n = 3$ case with the C_{3z} symmetry and perform first-principles calculations to demonstrate the existence of six intertwined Dirac-cone states and the QAHE with a high Chern number $C = 3$. As shown in Fig. 4a, the $\text{MnBi}_2\text{Te}_4/(\text{Bi}_2\text{Te}_3)_m/\text{MnBi}_2\text{Te}_4$ ($m = 0, 1, 2$) heterostructure is constructed by inserting m quintuple-layer Bi_2Te_3 between two MnBi_2Te_4 SLs, which preserves the required threefold rotational symmetry (C_{3z}) and the combined $M_x T$ symmetry. Moreover, according to the total energy calculation [49], the out-of-plane AFM order is preserved as the magnetic ground state of these heterostructures.

First, we inspect the evolution of the band structure of the $\text{MnBi}_2\text{Te}_4/\text{Bi}_2\text{Te}_3/\text{MnBi}_2\text{Te}_4$ heterostructure with increasing the strength of the out-of-plane electric field. Without the electric field, the band structure is doubly degenerate with an energy gap, as shown in Fig. 4b(i). Once a weak electric field is applied (e.g. $E = 0.008$

V/\AA), the band structure starts splitting due to breaking the PT symmetry, seen in Fig. 4b(ii). With increasing the electric field, the band structure undergoes two successive gap-closing-and-reopening processes, as can be seen from Figs. 4b(iii-vi), where the energy gap closes at $E = 0.0113 \text{ V/\AA}$ and $E = 0.0182 \text{ V/\AA}$, respectively.

Next, we investigate the topological properties, namely, Berry curvatures and corresponding Chern numbers for different regions of the electric field. The Chern number is calculated to be $C = 3$ in the intermediate region between the two gap-closing processes, whereas $C = 0$ for the other two regions (see the Wilson-loop [61] calculations in the SM [49]), which is well consistent with the above model prediction. Moreover, we have calculated the AHC as a function of the Fermi level in the $C = 3$ region, as shown in Fig. 4d, where the AHC takes the expected value of $\sigma_{xy} = 3 e^2/h$ when the Fermi level lies in the gap. This is further confirmed by the emergence of three chiral edge states in the energy gap (see Fig. 4e). To have a more intuitive picture of the above topological phase transitions, we have calculated the typical Berry curvatures for the three regions of the electric field, shown in Fig. 4f. We can see that significant changes of the Berry curvature occur around the points where intertwined Dirac cones are

located. This reflects the crucial role played by the intertwined Dirac cones in the topological phase transitions and the high-Chern-number QAHE. We also note that similar topological phase diagrams can be found for the $\text{MnBi}_2\text{Te}_4/(\text{Bi}_2\text{Te}_3)_m/\text{MnBi}_2\text{Te}_4$ heterostructure with $m = 0$, and $m = 2$, as shown in Fig. 4c (see the SM [49] for more details). To further validate our model analysis, apart from the $n = 3$ case, we also propose HgS and $\alpha\text{-Ag}_2\text{Te}$ thin films stacked along the (001) direction, through the magnetic proximity effect on the surfaces, for realizing the $n = 2$ and $n = 4$ cases hosting four and eight intertwined Dirac cones, respectively. Correspondingly, electrically tunable high-Chern-number phases of $C = 2$ and $C = 4$ are also confirmed by our first-principles calculations (see the SM [49]).

V. DISCUSSION AND CONCLUSION

In summary, we have considered the previously overlooked anisotropic coupling between Dirac-cone surface states of AFM TI thin films with n -fold rotational symmetry. Intriguingly, this coupling could lead to the emergence of $2n$ intertwined Dirac cones away from the Γ point in the presence of an out-of-plane electric field, and a high-Chern-number phase with $|C| = n$ is predicted by tuning the electric field, which has been explicitly demonstrated by the $C = 3$ QAHE phase of $\text{MnBi}_2\text{Te}_4/(\text{Bi}_2\text{Te}_3)_m/\text{MnBi}_2\text{Te}_4$ ($m = 0, 1, 2$) heterostructures from first-principles calculations.

The proposed intertwined Dirac-cone states are essentially different from conventional topological Dirac-cone surface state. The most unique advantage of the intertwined Dirac cones is the flexible electrical tunability, which could give rise to interesting physical phenomena. For example, the high-Chern-number phase in the AFM TI thin film can be used as an AFM switch controlled by an electric field, which may act as a prototypical low-power memory device for spintronic applications. Inspired by the recent development of twistrionics, a relative twist between the top and bottom surfaces of the AFM TI could result in flat bands with significantly reduced velocity of the intertwined Dirac-cone state, which may lead to high-Chern-number flat bands. More interestingly, the flat bands are expected to be greatly tuned by an electric field, which provides a new versatile platform for studying the interplay between topology, magnetism, twistrionics, and strong correlation effects.

This work is partly supported by National Key Projects for Research and Development of China (Grant No. 2021YFA1400400 and No. 2022YFA1403602), the Fundamental Research Funds for the Central Universities (Grant No. 020414380185), Natural Science Foundation of Jiangsu Province (No. BK20200007), and the Natural Science Foundation of China (No. 12074181, No. 12104217, No. 12174182, No. 12234011, No.

12374053, and No. 11834006). S. Murakami is supported by JSPS KAKENHI Grants No. JP22H00108 and No. JP22K18687 and MEXT Initiative to Establish Next-generation Novel Integrated Circuits Centers (X-NICS) Grant Number JPJ011438.

* Electronic address: zhanghj@nju.edu.cn; Electronic address: hqwang@nju.edu.cn

- [1] F. D. M. Haldane, Phys. Rev. Lett. **61**, 2015 (1988).
- [2] R. Yu, W. Zhang, H.-J. Zhang, S.-C. Zhang, X. Dai, and Z. Fang, Science **329**, 61 (2010).
- [3] C.-Z. Chang, J. Zhang, X. Feng, J. Shen, Z. Zhang, M. Guo, K. Li, Y. Ou, P. Wei, L.-L. Wang, et al., Science **340**, 167 (2013).
- [4] Y. Deng, Y. Yu, M. Z. Shi, Z. Guo, Z. Xu, J. Wang, X. H. Chen, and Y. Zhang, Science **367**, 895 (2020).
- [5] C.-Z. Chang, C.-X. Liu, and A. H. MacDonald, Rev. Mod. Phys. **95**, 011002 (2023).
- [6] X. Wan, A. M. Turner, A. Vishwanath, and S. Y. Savrasov, Phys. Rev. B **83**, 205101 (2011).
- [7] G. Xu, H. Weng, Z. Wang, X. Dai, and Z. Fang, Phys. Rev. Lett. **107**, 186806 (2011).
- [8] X.-L. Qi, T. L. Hughes, and S.-C. Zhang, Phys. Rev. B **78**, 195424 (2008).
- [9] L. Wu, M. Salehi, N. Koirala, J. Moon, S. Oh, and N. Armitage, Science **354**, 1124 (2016).
- [10] R. Li, J. Wang, X.-L. Qi, and S.-C. Zhang, Nat. Phys. **6**, 284 (2010).
- [11] D. M. Neno, C. A. Garcia, J. Gooth, C. Felser, and P. Narang, Nat. Rev. Phys. **2**, 682 (2020).
- [12] Y. Xiao, H. Wang, D. Wang, R. Lu, X. Yan, H. Guo, C.-M. Hu, K. Xia, H. Zhang, and D. Xing, Phys. Rev. B **104**, 115147 (2021).
- [13] T. Zhu, H. Wang, D. Xing, and H. Zhang, Phys. Rev. B **106**, 075103 (2022).
- [14] Y. Gong, J. Guo, J. Li, K. Zhu, M. Liao, X. Liu, Q. Zhang, L. Gu, L. Tang, X. Feng, et al., Chin. Phys. Lett. **36**, 076801 (2019).
- [15] M. M. Otrokov, I. I. Klimovskikh, H. Bentmann, D. Estyunin, A. Zeugner, Z. S. Aliev, S. Gass, A. U. B. Wolter, A. V. Koroleva, A. M. Shikin, et al., Nature **576**, 416 (2019).
- [16] D. Zhang, M. Shi, T. Zhu, D. Xing, H. Zhang, and J. Wang, Phys. Rev. Lett. **122**, 206401 (2019).
- [17] J. Li, Y. Li, S. Du, Z. Wang, B.-L. Gu, S.-C. Zhang, K. He, W. Duan, and Y. Xu, Sci. Adv. **5**, eaaw5685 (2019).
- [18] B. Chen, F. Fei, D. Zhang, B. Zhang, W. Liu, S. Zhang, P. Wang, B. Wei, Y. Zhang, Z. Zuo, et al., Nat. Commun. **10**, 4469 (2019).
- [19] Y. J. Chen, L. X. Xu, J. H. Li, Y. W. Li, H. Y. Wang, C. F. Zhang, H. Li, Y. Wu, A. J. Liang, C. Chen, et al., Phys. Rev. X **9**, 041040 (2019).
- [20] H. Li, S.-Y. Gao, S.-F. Duan, Y.-F. Xu, K.-J. Zhu, S.-J. Tian, J.-C. Gao, W.-H. Fan, Z.-C. Rao, J.-R. Huang, et al., Phys. Rev. X **9**, 041039 (2019).
- [21] Y.-J. Hao, P. Liu, Y. Feng, X.-M. Ma, E. F. Schwier, M. Arita, S. Kumar, C. Hu, R. Lu, M. Zeng, et al., Phys. Rev. X **9**, 041038 (2019).
- [22] M. M. Otrokov, I. P. Rusinov, M. Blanco-Rey, M. Hoff-

- mann, A. Y. Vyazovskaya, S. V. Ereemeev, A. Ernst, P. M. Echenique, A. Arnau, and E. V. Chulkov, *Phys. Rev. Lett.* **122**, 107202 (2019).
- [23] H. Sun, B. Xia, Z. Chen, Y. Zhang, P. Liu, Q. Yao, H. Tang, Y. Zhao, H. Xu, and Q. Liu, *Phys. Rev. Lett.* **123**, 096401 (2019).
- [24] J. Ge, Y. Liu, J. Li, H. Li, T. Luo, Y. Wu, Y. Xu, and J. Wang, *Nat. Sci. Rev.* **7**, 1280 (2020).
- [25] C. Hu, K. N. Gordon, P. Liu, J. Liu, X. Zhou, P. Hao, D. Narayan, E. Emmanouilidou, H. Sun, Y. Liu, et al., *Nat. Commun.* **11**, 97 (2020).
- [26] H. Wang, D. Wang, Z. Yang, M. Shi, J. Ruan, D. Xing, J. Wang, and H. Zhang, *Phys. Rev. B* **101**, 081109 (2020).
- [27] H. Fu, C.-X. Liu, and B. Yan, *Sci. Adv.* **6**, eaaz0948 (2020).
- [28] B. Lian, Z. Liu, Y. Zhang, and J. Wang, *Phys. Rev. Lett.* **124**, 126402 (2020).
- [29] P. M. Sass, J. Kim, D. Vanderbilt, J. Yan, and W. Wu, *Phys. Rev. Lett.* **125**, 037201 (2020).
- [30] C. Liu, Y. Wang, H. Li, Y. Wu, Y. Li, J. Li, K. He, Y. Xu, J. Zhang, and Y. Wang, *Nat. Mater.* **19**, 522 (2020).
- [31] M. Gu, J. Li, H. Sun, Y. Zhao, C. Liu, J. Liu, H. Lu, and Q. Liu, *Nat. Commun.* **12**, 3524 (2021).
- [32] H. Li, C.-Z. Chen, H. Jiang, and X. C. Xie, *Phys. Rev. Lett.* **127**, 236402 (2021).
- [33] A. Gao, Y.-F. Liu, C. Hu, J.-X. Qiu, C. Tzschaschel, B. Ghosh, S.-C. Ho, D. Bérubé, R. Chen, H. Sun, et al., *Nature* **595**, 521 (2021).
- [34] C. Liu, Y. Wang, M. Yang, J. Mao, H. Li, Y. Li, J. Li, H. Zhu, J. Wang, L. Li, et al., *Nat. Commun.* **12**, 4647 (2021).
- [35] T. Zhu, H. Wang, and H. Zhang, *Phys. Rev. B* **107**, 085151 (2023).
- [36] Y. Bai, Y. Li, J. Luan, R. Liu, W. Song, Y. Chen, P.-F. Ji, Q. Zhang, F. Meng, B. Tong, et al., *Nat. Sci. Rev.* **10**, nwad189 (2023).
- [37] N. Wang, D. Kaplan, Z. Zhang, T. Holder, N. Cao, A. Wang, X. Zhou, F. Zhou, Z. Jiang, C. Zhang, et al., *Nature* **621**, 487 (2023).
- [38] A. Gao, Y.-F. Liu, J.-X. Qiu, B. Ghosh, T. V. Trevisan, Y. Onishi, C. Hu, T. Qian, H.-J. Tien, S.-W. Chen, et al., *Science* **381**, 181 (2023).
- [39] T. Zhu, H. Wang, H. Zhang, and D. Xing, *npj Comput. Mater.* **7**, 121 (2021).
- [40] D. Wang, H. Wang, and H. Zhang, *Phys. Rev. B* **107**, 155114 (2023).
- [41] C.-X. Liu, X.-L. Qi, H. Zhang, X. Dai, Z. Fang, and S.-C. Zhang, *Phys. Rev. B* **82**, 045122 (2010).
- [42] W.-Y. Shan, H.-Z. Lu, and S.-Q. Shen, *New J. Phys.* **12**, 043048 (2010).
- [43] H.-Z. Lu, W.-Y. Shan, W. Yao, Q. Niu, and S.-Q. Shen, *Phys. Rev. B* **81**, 115407 (2010).
- [44] H.-P. Sun, C. M. Wang, S.-B. Zhang, R. Chen, Y. Zhao, C. Liu, Q. Liu, C. Chen, H.-Z. Lu, and X. C. Xie, *Phys. Rev. B* **102**, 241406 (2020).
- [45] C. Lei, S. Chen, and A. H. MacDonald, *Proc. Natl. Acad. Sci.* **117**, 27224 (2020).
- [46] D. Wang, H. Wang, D. Xing, and H. Zhang, *Sci. China-Phys. Mech. Astron.* **66**, 297211 (2023).
- [47] F. Viot, R. Hayn, M. Richter, and J. van den Brink, *Phys. Rev. Lett.* **106**, 236806 (2011).
- [48] W. Zhang, R. Yu, W. Feng, Y. Yao, H. Weng, X. Dai, and Z. Fang, *Phys. Rev. Lett.* **106**, 156808 (2011).
- [49] See the supplemental materials for the detailed derivation of the intertwined Dirac cones with their low-energy effective Hamiltonians, discussion of the neglected anisotropic coupling, the results for $n = 2, 4, 6$ cases, detailed band structures, Wilson loops, total energy calculations of $\text{MnBi}_2\text{Te}_4/(\text{Bi}_2\text{Te}_3)_m/\text{MnBi}_2\text{Te}_4$ ($m = 0, 1, 2$) heterostructures, and the detailed results of the realistic materials HgS and $\alpha\text{-Ag}_2\text{Te}$.
- [50] L. Fu, *Phys. Rev. Lett.* **103**, 266801 (2009).
- [51] G. Naselli, A. G. Moghaddam, S. Di Napoli, V. Vildosola, I. C. Fulga, J. van den Brink, and J. I. Facio, *Phys. Rev. Res.* **4**, 033198 (2022).
- [52] Z. S. Aliev, I. R. Amiraslanov, D. I. Nasonova, A. V. Shevelkov, N. A. Abdullayev, Z. A. Jahangirli, E. N. Orujlu, M. M. Otrokov, N. T. Mamedov, M. B. Babanly, et al., *J. Alloys Compd.* **789**, 443 (2019).
- [53] R. C. Vidal, A. Zeugner, J. I. Facio, R. Ray, M. H. Haghighi, A. U. B. Wolter, L. T. Corredor Bohorquez, F. Cagliaris, S. Moser, T. Figgemeier, et al., *Phys. Rev. X* **9**, 041065 (2019).
- [54] M. Z. Shi, B. Lei, C. S. Zhu, D. H. Ma, J. H. Cui, Z. L. Sun, J. J. Ying, and X. H. Chen, *Phys. Rev. B* **100**, 155144 (2019).
- [55] J. Wu, F. Liu, M. Sasase, K. Ienaga, Y. Obata, R. Yukawa, K. Horiba, H. Kumigashira, S. Okuma, T. Inoshita, et al., *Sci. Adv.* **5**, eaax9989 (2019).
- [56] D. Souchay, M. Nentwig, D. Günther, S. Keilholz, J. de Boor, A. Zeugner, A. Isaeva, M. Ruck, A. U. B. Wolter, B. Büchner, et al., *J. Mater. Chem. C* **7**, 9939 (2019).
- [57] X. Wu, J. Li, X.-M. Ma, Y. Zhang, Y. Liu, C.-S. Zhou, J. Shao, Q. Wang, Y.-J. Hao, Y. Feng, et al., *Phys. Rev. X* **10**, 031013 (2020).
- [58] R. C. Vidal, H. Bentmann, J. I. Facio, T. Heider, P. Kagerer, C. I. Fornari, T. R. F. Peixoto, T. Figgemeier, S. Jung, C. Cacho, et al., *Phys. Rev. Lett.* **126**, 176403 (2021).
- [59] W. Ge, J. Kim, Y.-T. Chan, D. Vanderbilt, J. Yan, and W. Wu, *Phys. Rev. Lett.* **129**, 107204 (2022).
- [60] X. Xu, S. Yang, H. Wang, R. Guzman, Y. Gao, Y. Zhu, Y. Peng, Z. Zang, M. Xi, S. Tian, et al., *Nat. Commun.* **13**, 7646 (2022).
- [61] A. Alexandradinata, X. Dai, and B. A. Bernevig, *Phys. Rev. B* **89**, 155114 (2014).

Supplemental Materials for “Intertwined Dirac cones induced by anisotropic coupling in antiferromagnetic topological insulator”

Yiliang Fan¹, Huaiqiang Wang^{2,*}, Peizhe Tang^{3,4}, Shuichi Murakami⁵, Xiangang Wan^{1,6}, Haijun Zhang^{1,6,*}, and Dingyu Xing^{1,6}

¹ *National Laboratory of Solid State Microstructures, School of Physics, Nanjing University, Nanjing 210093, China*

² *School of Physics and Technology, Nanjing Normal University, Nanjing 210023, China*

³ *School of Materials Science and Engineering, Beihang University, Beijing 100191, China*

⁴ *Max Planck Institute for the Structure and Dynamics of Matter, Center for Free Electron Laser Science, Hamburg 22761, Germany*

⁵ *Department of Physics, Tokyo Institute of Technology, Tokyo 152-8551, Japan*

⁶ *Collaborative Innovation Center of Advanced Microstructures, Nanjing University, Nanjing 210093, China*

*

Contents

I. Detailed solutions of the intertwined Dirac cones	1
II. Low-energy effective Hamiltonians of the intertwined Dirac cones	2
III. Discussion of the other neglected anisotropic coupling	3
IV. Berry curvatures and anomalous Hall conductivities of model with $n = 2, 4, 6$	4
V. The magnetic ground state of $\text{MnBi}_2\text{Te}_4/(\text{Bi}_2\text{Te}_3)_m/\text{MnBi}_2\text{Te}_4$ ($m = 0, 1, 2$)	4
VI. Wilson-loops of $\text{MnBi}_2\text{Te}_4/\text{Bi}_2\text{Te}_3/\text{MnBi}_2\text{Te}_4$	5
VII. Band structures, Wilson-loops, and edge states of $\text{MnBi}_2\text{Te}_4/(\text{Bi}_2\text{Te}_3)_m/\text{MnBi}_2\text{Te}_4$ ($m = 0, 2$)	5
VIII. Band structures, Wilson-loops of HgS and $\alpha\text{-Ag}_2\text{Te}$	5
References	6

I. DETAILED SOLUTIONS OF THE INTERTWINED DIRAC CONES

Here, we present the detailed solutions of the intertwined Dirac cones induced by the anisotropic coupling through solving the gap-closing points and critical potentials of the model Hamiltonian without/with the warping term. Without the warping term, the total Hamiltonian is given by

$$H_0 + H_{\text{coup}} = m\tau_z \otimes \sigma_z + u\tau_z \otimes \sigma_0 + v\tau_z \otimes (k_x\sigma_y - k_y\sigma_x) + (\Delta - Bk^2)\tau_x \otimes \sigma_0 + R_1g_n(k_x, k_y)\tau_y \otimes \sigma_0 \quad (\text{S1})$$

where $g_n(k_x, k_y) = (k_+^n - k_-^n)/2i$ and $k_{\pm} = k_x \pm ik_y$. To get the gap-closing points and critical potential, we must first solve the eigenvalue of the Hamiltonian, and the result is shown below

$$\epsilon_{\pm, \alpha} = \pm[m^2 + v^2k^2 + u^2 + (\Delta - Bk^2)^2 + R_1^2g_n^2 + 2(-1)^{\alpha-1}u\sqrt{m^2 + v^2k^2}]^{1/2}, \quad \alpha = 1, 2 \quad (\text{S2})$$

*Electronic address: zhanghj@nju.edu.cn; Electronic address: hqwang@nju.edu.cn

Next, we choose the two energy eigenvalues near the zero energy, i.e. $\epsilon_{\pm,2}$, and let them equal to each other $\epsilon_{+,2} = \epsilon_{-,2}$, we get the critical potential

$$u_0 = \left\{ m^2 + v^2 k^2 - (\Delta - Bk^2)^2 - R_1^2 g_n^2 + 2i \sqrt{(m^2 + v^2 k^2)[(\Delta - Bk^2)^2 + R_1^2 g_n^2]} \right\}^{1/2} \quad (S3)$$

Since the potential u_0 must be real, we naturally have the conditions:

$$\begin{cases} \Delta - Bk^2 = 0 \\ g_n = (k_+^n - k_-^n)/2i = k^n \sin(n\theta) = 0. \end{cases} \quad (S4)$$

Then we can get the gap-closing points (intertwined Dirac-cone points) from the above conditions and substitute them into the expression of u_0 to get the critical potential value. The final results are shown below:

$$\begin{cases} u_0 = \sqrt{m^2 + v^2 \Delta/B} \\ k_0 = \sqrt{\Delta/B} \\ \theta_j = j\pi/n, \quad j = 0, 1, \dots, 2n-1. \end{cases} \quad (S5)$$

When considering the warping term given by

$$H_{\text{warp}} = R_2 w_n(k_x, k_y) \tau_z \otimes \sigma_z, \quad (S6)$$

with $w_n(k_x, k_y) = (k_+^n + k_-^n)/2$, the solutions of the critical potential and gap-closing points can be obtained by substituting m in the above equations with $m(\mathbf{k}) = m + R_2 w_n(k_x, k_y)$. The results are then obtained as

$$\begin{cases} u_{0,j} = \sqrt{\left[m + (-1)^j R_2 (\Delta/B)^{n/2} \right]^2 + v^2 \Delta/B} \\ k_0 = \sqrt{\Delta/B} \\ \theta_j = j\pi/n, \quad j = 0, 1, \dots, 2n-1. \end{cases} \quad (S7)$$

II. LOW-ENERGY EFFECTIVE HAMILTONIANS OF THE INTERTWINED DIRAC CONES

First, we need to derive the two eigenstates of each intertwined Dirac cone located at $k = k_0$ and $\theta = \theta_j$ in the polar coordinates, which are given by

$$\begin{cases} \psi_+ = \left[\frac{-ie^{i\theta_j}(-m + \sqrt{m^2 + k_0^2 v^2})}{k_0 v}, 1, 0, 0 \right]^T \\ \psi_- = \left[0, 0, \frac{ie^{-i\theta_j}(-m + \sqrt{m^2 + k_0^2 v^2})}{k_0 v}, 1 \right]^T \end{cases} \quad (S8)$$

Then, by projecting the four-band full Hamiltonian in Eq. (S1) into the subspace expanded by the above two eigenstates, the two-band effective Hamiltonian up to linear order in momentum is then obtained as

$$\begin{aligned} h(\theta_j) &= \begin{bmatrix} \frac{\langle \psi_+ | H | \psi_+ \rangle}{|\langle \psi_+ | \psi_+ \rangle|} & \frac{\langle \psi_+ | H | \psi_- \rangle}{\sqrt{|\langle \psi_+ | \psi_+ \rangle| |\langle \psi_- | \psi_- \rangle|}} \\ \frac{\langle \psi_- | H | \psi_+ \rangle}{\sqrt{|\langle \psi_+ | \psi_+ \rangle| |\langle \psi_- | \psi_- \rangle|}} & \frac{\langle \psi_- | H | \psi_- \rangle}{|\langle \psi_- | \psi_- \rangle|} \end{bmatrix} \\ &= -2Bk_0 q_\rho \sigma_x + (-1)^j n R_1 k_0^{n-1} q_\theta \sigma_y + \delta u \sigma_z, \end{aligned} \quad (S9)$$

where $q_\rho = k - k_0$, $q_\theta = k_0 \delta\theta$ with $\delta\theta = \theta - \theta_j$, are the momentum measured from the nodal points along the radial and angular directions in the polar coordinates and $\delta u = u - u_0$. Obviously, this effective Hamiltonian describes a Dirac-cone state.

III. DISCUSSION OF THE OTHER NEGLECTED ANISOTROPIC COUPLING

Based on the theory of invariants [1], when considering all symmetry constraints imposed by the preserved C_{nz} [$=\exp(-\frac{i\pi}{n}\sigma_z)$], PT [$=\tau_x \otimes i\sigma_y K$], and $M_x T$ [$= -i\sigma_z K$] symmetries, the most general symmetry-allowed coupling Hamiltonian can be obtained as

$$H_{\text{coup}} = (\Delta - Bk^2)\tau_x \otimes \sigma_0 + R_1 \frac{k_+^n - k_-^n}{2i} \tau_y \otimes \sigma_0 + R_3 \frac{k_+^n + k_-^n}{2} \tau_x \otimes \sigma_0 \quad (\text{S10})$$

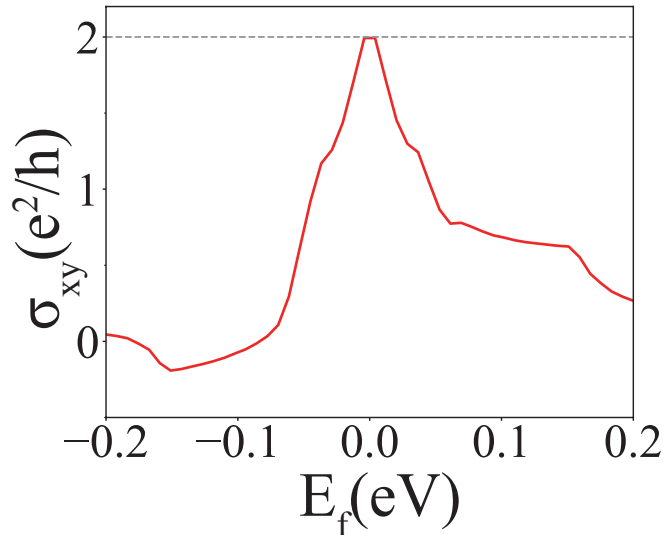


Fig. S1: **Anomalous Hall conductivity for the $n = 2$ case with the neglected R_3 coupling term when $u_- < u < u_+$.** The parameters are chosen as $u = 0.1$ eV, $m = 0.05$ eV, $v = 1$ eV $\cdot \text{\AA}$, $\Delta = 0.05$ eV, $B = 5$ eV $\cdot \text{\AA}^2$, $R_1 = 10$ eV $\cdot \text{\AA}^2$, $R_2 = 10$ eV $\cdot \text{\AA}^2$, $R_3 = 2$ eV $\cdot \text{\AA}^2$ in the above numerical calculations.

Apart from the first two terms discussed in the main text, the third higher-order coupling R_3 term is also symmetry-allowed which is neglected in the main text for simplicity. Here, we will show that it will not affect the main results of our work. We take the $n = 2$ case with the full Hamiltonian written as

$$H = m(\mathbf{k})\tau_z \otimes \sigma_z + v\tau_z \otimes (k_x\sigma_y - k_y\sigma_x) + \Delta(\mathbf{k})\tau_x \otimes \sigma_0 + R_1 g_n(k_x, k_y)\tau_y \otimes \sigma_0, \quad (\text{S11})$$

where $m(\mathbf{k}) = m + R_2(k_x^2 - k_y^2)$, and $\Delta(\mathbf{k}) = \Delta - Bk^2 + R_3(k_x^2 - k_y^2)$. Through a similar procedure as above, we can find the critical potential and the intertwined Dirac cones as

$$\begin{cases} u_+ \equiv u_j = \sqrt{\left(m + \frac{\Delta R_2}{B - R_3}\right)^2 + \frac{v^2 \Delta}{B - R_3}} \\ k_j = \sqrt{\frac{\Delta}{B - R_3}} \\ \theta_j = j\pi/2, \quad j = 0, 2 \end{cases} \quad (\text{S12})$$

and

$$\begin{cases} u_- \equiv u_j = \sqrt{\left(m - \frac{\Delta R_2}{B + R_3}\right)^2 + \frac{v^2 \Delta}{B + R_3}} \\ k_j = \sqrt{\frac{\Delta}{B + R_3}} \\ \theta_j = j\pi/2, \quad j = 1, 3 \end{cases} \quad (\text{S13})$$

As we can see, if $R_3 < B$ is satisfied, there are still two successive gap-closing processes at u_- and u_+ , respectively, and the calculation of anomalous Hall conductivity (AHC) [shown in Fig. S1] confirms that there is a high-Chern-number phase ($|C| = 2$) between u_- and u_+ . However, due to the nonzero R_3 term, the gap-closing points are no

longer located on the circle with radius $k_0 = \sqrt{\Delta/B}$. In contrast, if $R_3 > B$, $k_j = \sqrt{\Delta/(B - R_3)}$ with $j = 0, 2$ will not exist, indicating that there will not be another gap-closing process occurring at $u = u_+$. As a result, there exists an upper critical value of R_3 for the emergence of the intermediate high-Chern-number state. Nevertheless, the R_3 coupling term does not fundamentally affect the results in the main text and is thus reasonably neglected for simplicity.

IV. BERRY CURVATURES AND ANOMALOUS HALL CONDUCTIVITIES OF MODEL WITH $n = 2, 4, 6$

In addition to the $n = 3$ case in the main text, here, we show the numerical calculations of the Berry curvatures and anomalous Hall conductivities for the $n = 2$ (first row), $n = 4$ (second row), and $n = 6$ (third row) cases in Fig. S2.

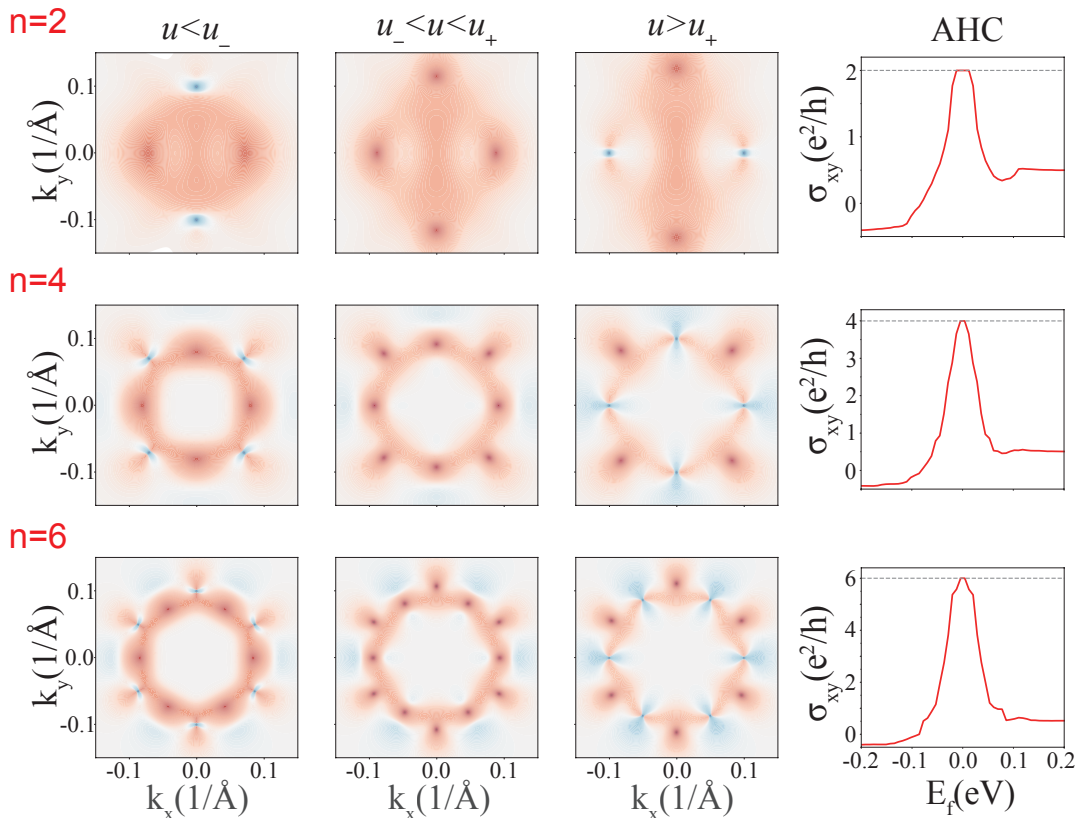


Fig. S 2: **Berry curvatures and anomalous Hall conductivities of model with $n = 2, 4, 6$.** The parameters are chosen as $m = 0.05$ eV, $v = 1$ eV \cdot \AA , $\Delta = 0.05$ eV, $B = 5$ eV \cdot \AA^2 , $R_1 = 10^{n-1}$ eV \cdot \AA^n , $R_2 = 10^{n-1}$ eV \cdot \AA^n in the above numerical calculations.

V. THE MAGNETIC GROUND STATE OF $\text{MnBi}_2\text{Te}_4/(\text{Bi}_2\text{Te}_3)_m/\text{MnBi}_2\text{Te}_4$ ($m = 0, 1, 2$)

Here, we only consider the magnetic order with Mn atoms' magnetic moments towards the out-of-plane direction. We compare the energy per cell of $\text{MnBi}_2\text{Te}_4/(\text{Bi}_2\text{Te}_3)_m/\text{MnBi}_2\text{Te}_4$ ($m = 0, 1, 2$) with ferromagnetic (FM) order and antiferromagnetic (AFM) order. The results are listed in Table S1. As shown in Table S1, for $m=0,1,2$, the energy per cell of the AFM order is lower than FM order of 1.46 meV, 0.19 meV and 0.05 meV separately, which verifies that the AFM order state is the magnetic ground state of $\text{MnBi}_2\text{Te}_4/(\text{Bi}_2\text{Te}_3)_m/\text{MnBi}_2\text{Te}_4$ ($m = 0, 1, 2$).

m	FM Energy	AFM Energy
0	0 meV	-1.46 meV
1	0 meV	-0.19 meV
2	0 meV	-0.05 meV

Table S 1: **Energy per cell of $\text{MnBi}_2\text{Te}_4/(\text{Bi}_2\text{Te}_3)_m/\text{MnBi}_2\text{Te}_4$ ($m = 0, 1, 2$) with out-of-plane FM and AFM magnetic order.** The energy of the FM order is set to be zero and the energy of the AFM order is compared to that of FM.

VI. WILSON-LOOPS OF $\text{MnBi}_2\text{Te}_4/\text{Bi}_2\text{Te}_3/\text{MnBi}_2\text{Te}_4$

Here, we show the calculation of the Chern number of $\text{MnBi}_2\text{Te}_4/\text{Bi}_2\text{Te}_3/\text{MnBi}_2\text{Te}_4$ by Wilson-loop methods (the Wilson-loop winding number equals to the Chern number [2]) under different electric field values in Fig. S3. As shown in Fig. S3, when $E = 0.011 \text{ V/\AA}$, the Wilson-loop winding number is 0, when $E = 0.0135 \text{ V/\AA}$, the Wilson-loop winding number is 3, and when $E = 0.0186 \text{ V/\AA}$, the Wilson-loop winding number returns to 0.

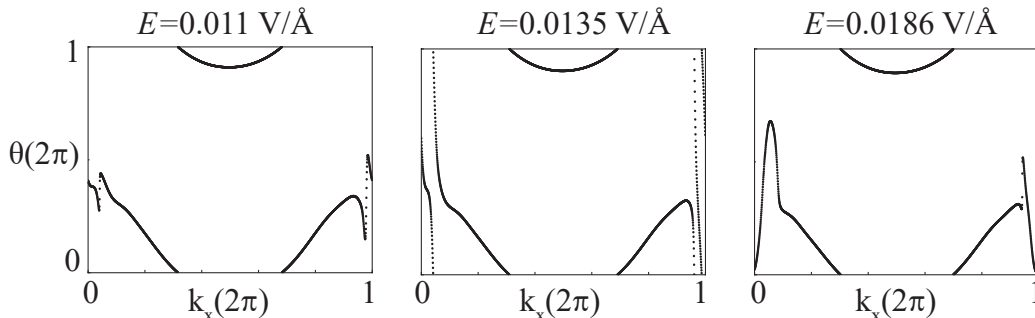


Fig. S 3: **Wilson-loops of $\text{MnBi}_2\text{Te}_4/(\text{Bi}_2\text{Te}_3)/\text{MnBi}_2\text{Te}_4$ under different electric fields.** The electric fields are $E = 0.011 \text{ V/\AA}$, $E = 0.0135 \text{ V/\AA}$, and $E = 0.0186 \text{ V/\AA}$.

VII. BAND STRUCTURES, WILSON-LOOPS, AND EDGE STATES OF $\text{MnBi}_2\text{Te}_4/(\text{Bi}_2\text{Te}_3)_m/\text{MnBi}_2\text{Te}_4$ ($m = 0, 2$)

Here, we show that band structures, Wilson-loops, and edge states of $\text{MnBi}_2\text{Te}_4/(\text{Bi}_2\text{Te}_3)_m/\text{MnBi}_2\text{Te}_4$ ($m = 0, 2$) in Fig. S4 to exhibit the 0-3-0 transition of Chern number of them. Fig. S4a shows band structures of $\text{MnBi}_2\text{Te}_4/(\text{Bi}_2\text{Te}_3)_m/\text{MnBi}_2\text{Te}_4$ ($m = 0, 2$) under different electric fields. For the $m = 0$ ($m = 2$) case, the energy gap closes at $E = 0.0148 \text{ V/\AA}$ ($E = 0.0078 \text{ V/\AA}$) and reopens when the electric field continues to increase, and when $E = 0.0168 \text{ V/\AA}$ ($E = 0.0125 \text{ V/\AA}$), the gap closes again. Fig. S4c shows the calculation of the Wilson-loops for the $m = 0$ and $m = 2$ cases when $E = 0.0162 \text{ V/\AA}$ and $E = 0.01 \text{ V/\AA}$, respectively, both of which exhibit a Wilson-loop winding number of 3. It confirms the existence of a high-Chern-number phase with $C = 3$. Fig. S4b shows the edge states of $m = 0$ and $m = 2$ case when $E = 0.0162 \text{ V/\AA}$ and $E = 0.01 \text{ V/\AA}$ respectively, verifying the Chern number is indeed 3.

VIII. BAND STRUCTURES, WILSON-LOOPS OF HgS AND $\alpha\text{-Ag}_2\text{Te}$

We choose HgS and $\alpha\text{-Ag}_2\text{Te}$ as realistic materials for the $n = 2$ and $n = 4$ cases, respectively, in our model discussions. HgS is a topological insulator respecting C_{2z} symmetry [3]. $\alpha\text{-Ag}_2\text{Te}$ is a zero-gap semiconductor respecting C_{4z} symmetry with inverted band structure [4], and we have applied a tensile in-plane strain resulting in $c/a = 0.97$ ($c/a = 1$ before applying strain) to open a small gap at the Γ point. Moreover, since HgS and $\alpha\text{-Ag}_2\text{Te}$ are non-magnetic, we have constructed a several-cell-slab tight-binding model along the out-of-plane direction based on first-principles calculations of the bulk electronic structures and suppose there are two ferromagnetic materials with opposite magnetic moments near the top and bottom surfaces of the slab separately. To simulate the magnetic proximity effect induced by the two ferromagnetic materials, we then add opposite zeeman coupling energies to the top (0.05 eV) and bottom (-0.05 eV) cells, respectively. Finally, the potential imposed by the out-of-plane electric field is simulated by adding the onsite potential to each cell according to its coordinates along the stacking direction.

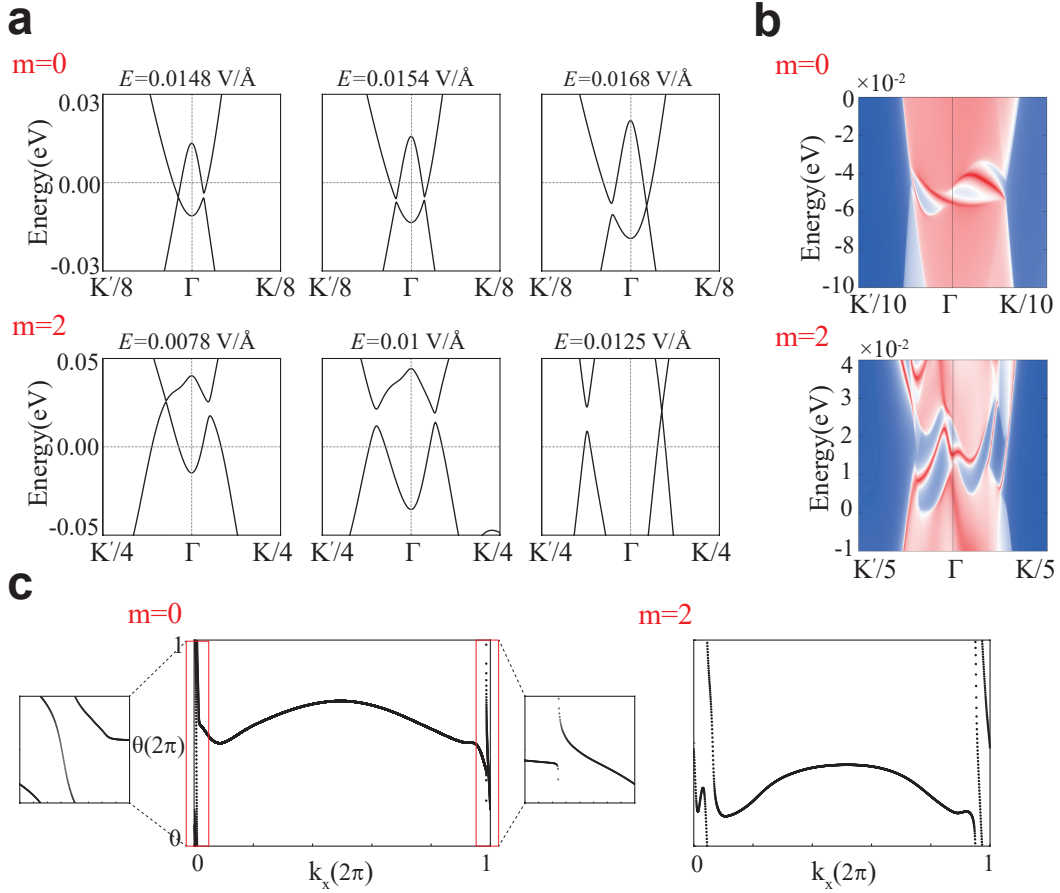


Fig. S 4: **Band structures, Wilson-loops, and edge states of $\text{MnBi}_2\text{Te}_4/(\text{Bi}_2\text{Te}_3)_m/\text{MnBi}_2\text{Te}_4$ ($m = 0, 2$).** (a) Band structures of $\text{MnBi}_2\text{Te}_4/(\text{Bi}_2\text{Te}_3)_m/\text{MnBi}_2\text{Te}_4$ ($m = 0, 2$) under different electric fields: $E = 0.0148 \text{ V/\AA}$, $E = 0.0154 \text{ V/\AA}$, $E = 0.0168 \text{ V/\AA}$ for $m = 0$; $E = 0.0078 \text{ V/\AA}$, $E = 0.01 \text{ V/\AA}$, $E = 0.0125 \text{ V/\AA}$ for $m = 2$. (b) Edge states of $\text{MnBi}_2\text{Te}_4/(\text{Bi}_2\text{Te}_3)_m/\text{MnBi}_2\text{Te}_4$ ($m = 0, 2$) when $E = 0.0168 \text{ V/\AA}$ ($m = 0$) and $E = 0.01 \text{ V/\AA}$ ($m = 2$). (c) Wilson-loops of $\text{MnBi}_2\text{Te}_4/(\text{Bi}_2\text{Te}_3)_m/\text{MnBi}_2\text{Te}_4$ ($m = 0, 2$) when $E = 0.0168 \text{ V/\AA}$ ($m = 0$) and $E = 0.01 \text{ V/\AA}$ ($m = 2$).

For HgS , we build a 5-cell-slab tight-binding model, as shown in Fig. S5a. Figure S5b shows the band structures of the model under different electric fields, where the high-symmetry points M_1, M_2 are labeled in Fig. S5c, we find that the energy gap closes at $E_- = 0.0233 \text{ V/\AA}$ and $E_+ = 0.0384 \text{ V/\AA}$. Between E_- and E_+ , there is a $|C| = 2$ phase, which is verified by calculating the Wilson-loops at $E = 0.02 \text{ V/\AA}$ ($< E_-$), 0.03 V/\AA (between E_- and E_+) and 0.04 V/\AA ($> E_+$) in Fig. S5d. As shown in Fig. S5d, apparently, when $E < E_-$ and $E > E_+$, the Wilson-loop winding number is 0, but when $E_- < E < E_+$, the Wilson-loop winding number is 2.

For $\alpha\text{-Ag}_2\text{Te}$, we build a 4-cell-slab model, as shown in Fig. S6a. The band structure evolution of $\alpha\text{-Ag}_2\text{Te}$ with different electric fields is shown in Fig. S6b, where the energy gap closes at $E_- = 0.027 \text{ V/\AA}$ and $E_+ = 0.039 \text{ V/\AA}$. Figure S6d shows the results of Wilson-loops at $E = 0.02 \text{ V/\AA}$ ($< E_-$), 0.03 V/\AA (between E_- and E_+) and 0.04 V/\AA ($> E_+$), which confirms the existence of the high-Chern-number phase with $|C| = 4$ induced by the intertwined Dirac cones.

-
- [1] C.-X. Liu, X.-L. Qi, H. Zhang, X. Dai, Z. Fang, and S.-C. Zhang, Phys. Rev. B **82**, 045122 (2010).
 - [2] A. Alexandradinata, X. Dai, and B. A. Bernevig, Phys. Rev. B **89**, 155114 (2014).
 - [3] F. Viot, R. Hayn, M. Richter, and J. van den Brink, Phys. Rev. Lett. **106**, 236806 (2011).
 - [4] W. Zhang, R. Yu, W. Feng, Y. Yao, H. Weng, X. Dai, and Z. Fang, Phys. Rev. Lett. **106**, 156808 (2011).

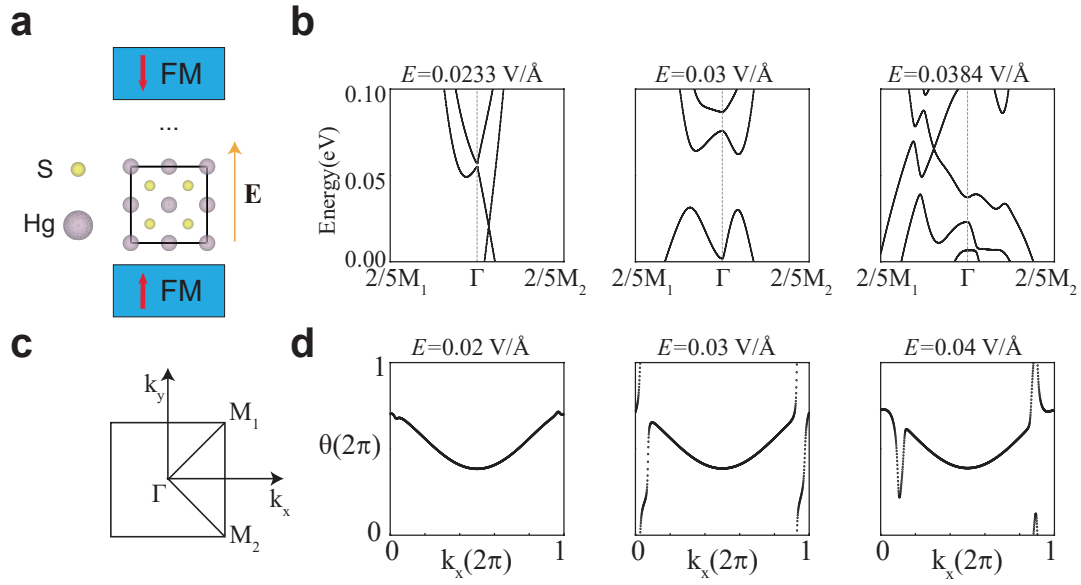


Fig. S 5: **Structure, band structures, and Wilson-loops of the five-cell-slab model of HgS with opposite Zeeman energies in the top and bottom cell.** (a) Structure of the slab model of HgS. (b) Band structures under different electric fields of 0.0233 V/Å, 0.03 V/Å, and 0.0384 V/Å. (c) Two-dimensional Brillouin zone of the slab and the high-symmetry points. (d) Wilson-loops under different electric fields of 0.02 V/Å, 0.03 V/Å, and 0.04 V/Å.

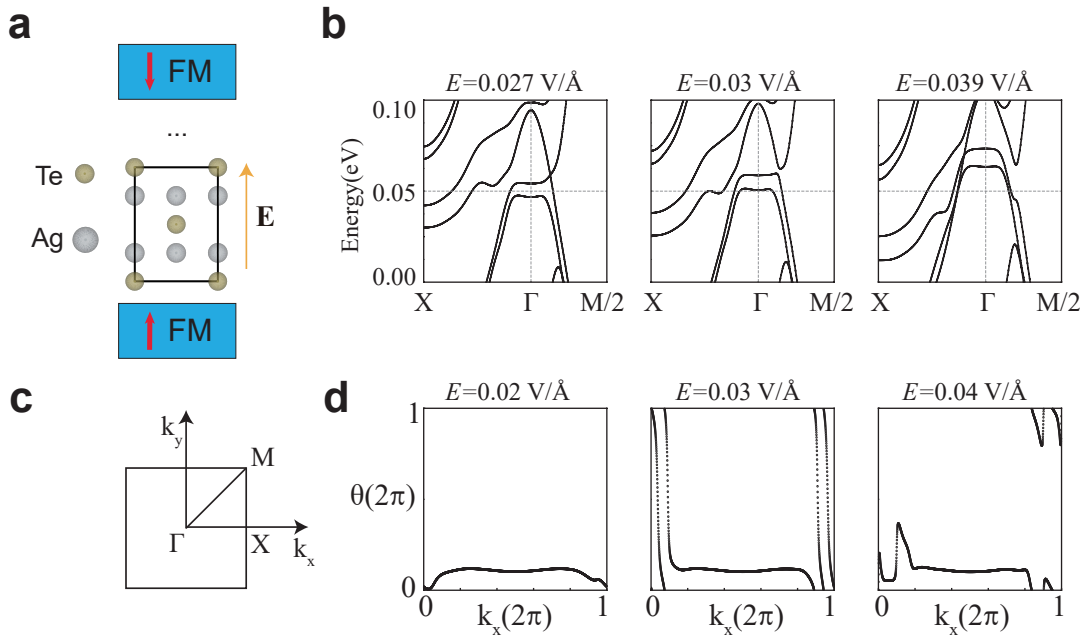


Fig. S 6: **Structure, band structures, and Wilson-loops of four-cell-slab model of α -Ag₂Te with opposite Zeeman energy in the top and bottom cell.** (a) Structure of slab model of α -Ag₂Te. (b) Band structures under different electric fields of 0.027 V/Å, 0.03 V/Å, 0.039 V/Å. (c) Two-dimensional Brillouin zone of the slab and the high-symmetry points. (d) Wilson-loops under different electric fields of 0.02 V/Å, 0.03 V/Å, 0.04 V/Å.